Journal of
Micro/Nanolithography,
MEMS, and MOEMS

Nanolithography.SPIEDigitalLibrary.org

Phase defect detection signal analysis: dependence of defect size variation

Tsuyoshi Amano
Hidehiro Watanabe
Tsukasa Abe

SPIE.

Phase defect detection signal analysis: dependence of defect size variation

Tsuyoshi Amano,[a,*] Hidehiro Watanabe,[a] and Tsukasa Abe[b]
[a]EUVL Infrastructure Development Center, Inc., 16-1 Onogawa, Tsukuba, Ibaraki 305-8569, Japan
[b]Dai Nippon Printing Co., Ltd., 2-2-1 Fukuoka, Fujimino, Saitama 356-8507, Japan

Abstract. The influence of the size or volume of the phase defect embedded in the extreme ultraviolet mask on wafer printability by scanning probe microscope (SPM) is well studied. However, only a few experimental results on the measurement accuracy of the phase defect size have been reported. Therefore, in this study, the measurement repeatability of the phase defect volume using SPM and the influence of the defect volume distribution on defect detection signal intensity (DSI) using an at-wavelength dark-field defect inspection tool were examined. A programmed phase defect mask was prepared, and a defect size measurement repeatability test was conducted using an SPM. As a result, the variation of the measured volume due to the measurement repeatability was much smaller than that of the defect-to-defect variation. This result indicates that measuring the volume of each phase defect is necessary in order to evaluate the defect detection yield using a phase defect inspection tool and wafer printability. In addition, the images of phase defects were captured using an at-wavelength dark-field inspection tool from which the defect DSIs were calculated. The DSI showed a direct correlation with the defect volume. © *The Authors. Published by SPIE under a Creative Commons Attribution 3.0 Unported License. Distribution or reproduction of this work in whole or in part requires full attribution of the original publication, including its DOI.* [DOI: 10.1117/1.JMM.14.1.013502]

Keywords: extreme ultraviolet; phase defect; inspection; defect mitigation.

Paper 14159P received Nov. 7, 2014; accepted for publication Dec. 29, 2014; published online Jan. 22, 2015.

1 Introduction

Extreme ultraviolet lithography (EUVL) is considered to be the most promising next-generation lithography after the point where 193-nm immersion lithography will not be able to deliver smaller features. However, the path to establish the EUVL is not without technical difficulties. For example, the lack of sufficient light-source power, particle-free mask handling, defect-free and flat mask blanks,[1–5] and resist material development[6,7] need to be resolved. From the viewpoint of EUV mask fabrication, mask pattern defect inspection[8–10] and repair[11–13] are some of the most demanding tasks to be addressed. The reason is that for the EUVL generation, the device pattern feature size happens to be exceedingly small and calls for a higher repairing accuracy than would be required in optical lithography.[14–16] Regarding the types of defects, the nature of the pattern defects in the EUV mask is mostly the same as in the case of optical masks except for those defects that are classified as reflective multilayer defects, such as bump or pit phase defects that propagate through the multilayer during its deposition on the substrate surface, which are hard to repair.[17] Therefore, to reduce the effect of a phase defect on the wafer printing image, two elimination methods are suggested. One method is to cover the phase defects beneath an absorber pattern by shifting the position of the device pattern during mask patterning.[18–20] The other is to eliminate the influence of the phase error by removing the absorber away from close proximity to the phase defects after fabricating the device pattern.[21] In order to make these methods succeed, it is necessary to measure the size or volume of the phase defects using a scanning probe microscope (SPM) or an at-wavelength defect inspection tool.[22–24] The at-wavelength defect inspection tool has considerable advantages over the other defect inspection tools which are limited to deep ultraviolet light optics. An advantage of employing the EUV light is not only limited to the tool's excellent capability of detecting phase defects, but also of predicting the lithographic impact of the detected phase defect on wafers.[25–29]

*Address all correspondence to: Tsuyoshi Amano, E-mail: tsuyoshi.amano@eidec.co.jp

2 Experiment

2.1 *Preparation of a Programmed Phase Defect EUV Blank*

A programmed pit phase defect EUV blank without any absorber layer was prepared. The EUV blank used in this study consisted of a Ru-capped Mo/Si multilayer deposited on a quartz substrate. The multilayer consisted of 2.5-nm-thick layer of Ru and 40-bilayer Mo (2.2-nm thick)/Si (4.8-nm thick). Seeds for phase defects on a quartz substrate comprising holes of 50, 60, 70, 80, and 100 nm in diameter were fabricated through resist patterning and quartz dry etching processes. Phase defects arrayed in 5×2 matrices with their pitch values of 5 μm surrounded by guide patterns of half pitch 100-nm lines and spaces were fabricated on a quartz substrate (Fig. 1). As a first step, a photoresist layer was coated on a chrome layer previously sputtered on the quartz substrate. Next, a set of seeds for the phase defects and the guide patterns were drawn on the photoresist layer by an electron-beam writing tool (JBX-9300FS, JEOL Ltd, Tokyo, Japan). Then after developing the photoresist layer, the chrome layer and the quartz substrate were etched. As a last step, the chrome layer was removed. After running through a cleaning process, the patterned substrate was then coated with a Ru-capped multilayer.

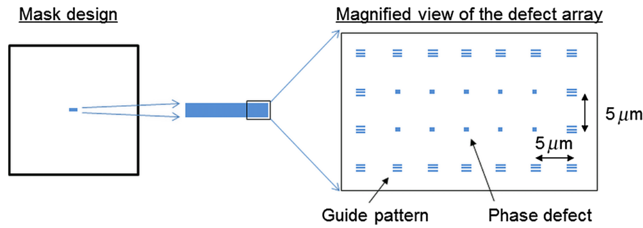

Fig. 1 Arrangement of the programmed phase defects and the guide patterns.

2.2 *Measurement of the Phase Defect Volume*

The volumes of the phase defects were measured using an SPM (L-Trace II, Hitachi High-Tech Science Corp., Tokyo, Japan). The cantilevers used in this study employed a triangular pyramid shaped tip (SI-DF40P2, Hitachi High-Tech Science Corp., Tokyo, Japan). A probe material made of Si with a spring constant of 26 N/m was incorporated into the cantilever. The typical values of the resonant frequency and tip radius of curvature were 300 kHz and 7 nm. The scan area and speed were set to 600×600 nm and 1.7 Hz. The numbers of the image pixels were 512 or 1024 points for the X direction, and 128, 256, 512, and 1024 points for the Y direction. After capturing the SPM image, the defect volume was calculated as illustrated in Fig. 2. Figure 2(a) shows the SPM image of the multilayer surface that includes the phase defect. To eliminate the volume of the reference area that is caused by the multilayer surface roughness from the phase defect volume, a setting of an adequate datum plane was made. As the first step, a masking area, in other words an area that includes the phase defect, was set to calculate the datum plane as shown in Fig. 2(b). Figure 2(c) shows the SPM image of the multilayer surface with the masking area. Figure 2(d) represents a histogram of the pixel heights of Fig. 2(c). The datum plane was set to the total volumes of the above and below the datum plane that corresponded to the areas A and B in Fig. 2(d) so that they were equal. The removed phase defect shown in Fig. 2(b) was put back in place while taking into account the datum plane adjustment. A histogram of the pixel heights of Fig. 2(e) is shown in Fig. 2(f). The histogram curve greater than 0 nm in height was changed from red to blue [Fig. 2(g)]. An area C in Fig. 2(g), bounded by the horizontal axis, vertical axis, and the blue curve greater than 0 nm in height, corresponds to the total volume of the surface roughness above the datum plane, whereas the area A in Fig. 2(d) excludes the masking area from the calculation of the volume of the surface roughness. An area D represents an axisymmetric domain of the area C. As prescribed, after setting an adequate datum plane, the total volume of the surface roughness below the datum plane, expressed in the area D, is equal to the volume expressed in the area C. The volume below the datum plane includes the volume of the phase defect and the reference area. Therefore, the area E in Fig. 2(g), subtracted the area D from the volume below the datum plane, corresponds to the volume of the phase defect.

2.3 *Phase Defect Inspection Tool*

The phase defects were acquired in images using an actinic blank inspection (ABI) high-volume manufacturing (HVM) model (Lasertec Corporation, Yokohama, Japan). The image acquisitions were done both ways: inspection mode and review mode as described below. Figure 3 shows a schematic model of an ABI HVM optics. The ABI HVM operates in two imaging modes. One is a high speed EUV blank inspection mode that employs a Schwarzschild optics with a magnification of 26× as shown in Fig. 3(a).[23,25] The other imaging mode is a high magnification of 1200× review mode that employs a switch mirror and a second concave mirror after the Schwarzschild optics as shown in Fig. 3(b). The EUV light scattered by a phase defect on the EUV blank is captured by the Schwarzschild optics and detected by a charge-coupled device (CCD) camera. The inner and outer

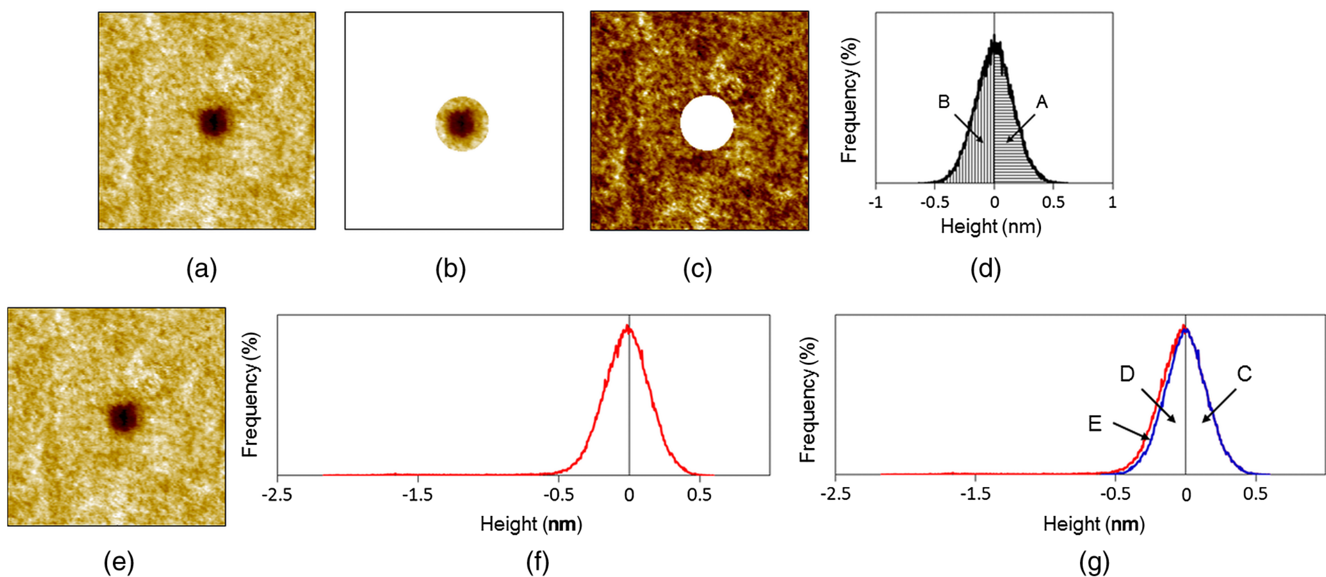

Fig. 2 Calculation method of the phase defect volume: (a) a captured SPM image; (b) choosing an area of the phase defect (setting a masking area); (c) calculating a datum plane of the multilayer without the phase defect area; (d) histogram of the pixel height of the image (c); (e) putting the phase defect back in place; (f) and (g) histograms of the pixel heights of the image (e).

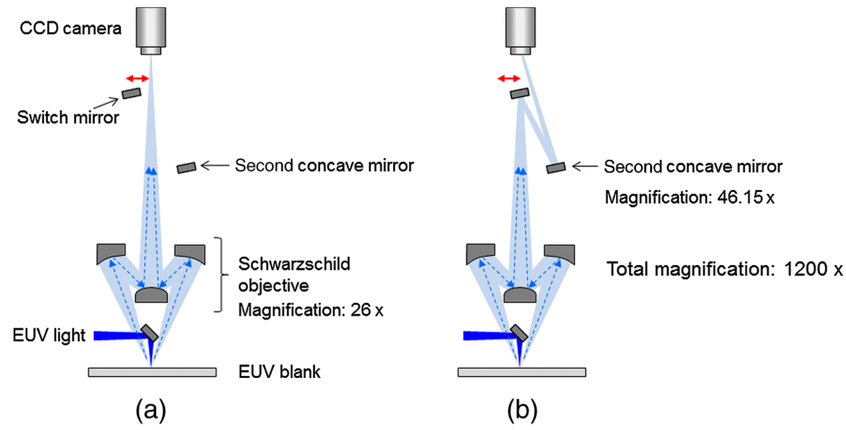

Fig. 3 Schematic view of the optics of the inspection tool: (a) phase defect inspection mode; (b) high magnification phase defect review mode.

numerical apertures of the Schwarzschild optics are 0.1 and 0.27, respectively. The pixel size of the CCD camera at the EUV blank plane was 462 nm in the 26× inspection mode and 10 nm in the 1200× review mode.

3 Results and Discussions

3.1 *Measurement Repeatability of the Phase Defect Volume Using SPM*

The first step to determine the measurement condition of the phase defect volume using the SPM was carried out by evaluating the repeatability of the phase defect volume as a function of the image pixel size. The measurement conditions are summarized in Table 1. The entire SPM imaging was conducted on a phase defect without changing the tip. At first, 10 consecutive SPM images were taken under the condition of the measurement ID 1 in Table 1. Next, 10 consecutive SPM images were taken under the condition of the measurement ID 2, and so on. The condition of the measurement ID 5 is same as the condition of the ID 1. The mean value and variation of the measured volumes as functions of the image pixel size are summarized in Fig. 4. From the view point of the SPM imaging, a smaller number of scan lines is preferred because a larger number of scan line takes a longer SPM imaging time and is also prone to tip damage. The experimental results indicated that because of the large pixel size, the condition of the measurement ID 2 was not suitable for the measurement since the variation of the measured volume was obviously larger than that of the other measurement IDs involved. On the other hand, the pixel sizes below X: 1.17 and Y: 2.34 nm had little impact on the volume and on the variation of the defect size measurement. Therefore, in this work, the pixel sizes of X: 1.17 and Y: 2.34 nm that correspond to X: 512 and Y: 256 pixels were selected to capture the images of the phase defects.

The second step to evaluate the measurement repeatability of the phase defect volume was carried out by capturing 20 consecutive SPM images. Figures 5(a) and 5(b) show, as functions of the SPM imaging times, the measured volume of a phase defect and the surface roughness of the root-mean-square value without the phase defect area as shown in Fig. 2(c). The measured volume of the phase defect fluctuated between 3000 and 3500 nm^3 through 20 consecutive measurements. The measured surface roughness also showed fluctuation. Generally, the surface roughness value begins to give smaller readings as the tip radius becomes dull in relation to the surface structures of the object of measurement. In any case, the tip is assumed to retain its sharpness for long enough in order to measure the multilayer surface. The relationship between the measured surface roughness and defect volume is shown in Fig. 5(c). This result indicates that there was no identifiable relationship between the measured surface roughness and the measured volume, and indicates that we cannot tell whether the tip is sharp or dull from the roughness value. The distributions of the measured defect volumes

Table 1 Number of the scanning probe microscope imaging pixels of X and Y directions and their pixel size.

Measurement ID		1	2	3	4	5
Number of pixels	X	512	512	512	1024	512
	Y	256	128	512	1024	256
Pixel size (nm/pixel)	X	1.17	1.17	1.17	0.59	1.17
	Y	2.34	4.68	1.17	0.59	2.34

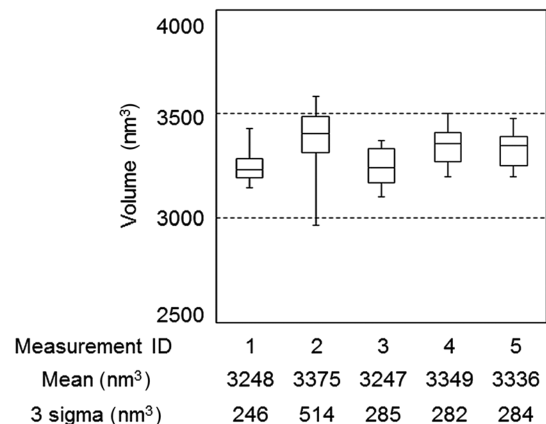

Fig. 4 Box-plots of the measured phase defect volumes.

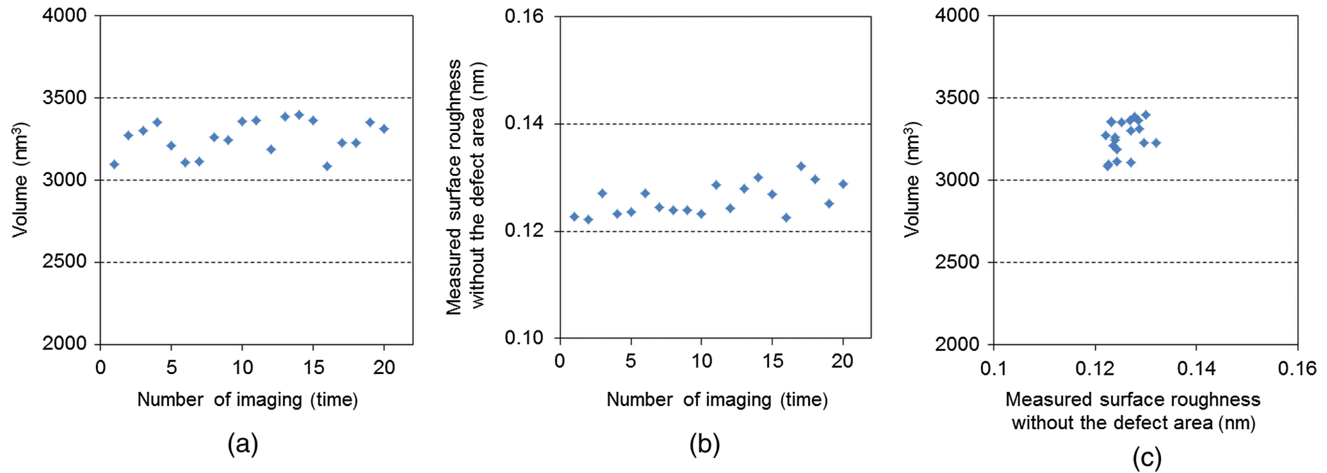

Fig. 5 Calculated results of the phase defect volume and the surface roughness of the multilayer from the scanning probe microscope images: (a) phase defect volume as a function of the imaging time; (b) surface roughness of the multilayer without phase defect area as a function of the imaging time; (c) relationship between the measured surface roughness and defect volume.

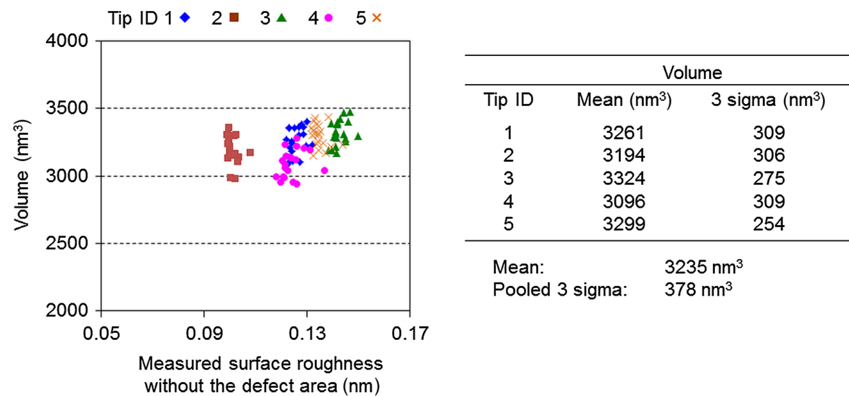

	Volume	
Tip ID	Mean (nm³)	3 sigma (nm³)
1	3261	309
2	3194	306
3	3324	275
4	3096	309
5	3299	254

Mean: 3235 nm³
Pooled 3 sigma: 378 nm³

Fig. 6 Measured defect volume as a function of the surface roughness.

indicate the measurement repeatability of the phase defect volume using the SPM employed in this study.

The influence of the difference in the tip on the measured defect volume was also evaluated. A phase defect was captured by taking 20 consecutive SPM images with five brand-new tips each time. Figure 6 shows a relationship between the measured surface roughness without the defect area and defect volume. The variations of measured volumes of tip-to-tip are smaller than those of 20 continuous measurements. As prescribed, the tip-to-tip test also indicated that there is little relationship between the roughness value and defect volume. These results show that multiple volume measurements are useful in evaluating the defect capturing yield.

3.2 *Influence of the Defect Volume on the Defect Signal Intensity*

In this section, the influence of the phase defect volume on the ABI HVM defect signal intensity (DSI) is described. Each phase defect, as explained in Sec. 2.1, was measured for its volume five times using SPM. The phase defect images were also acquired five times using the 26× inspection optics of ABI HVM. The exposure time for all images was 40.5 ms. Figure 7(a) shows the relationship between the volumes of the phase defects and the DSIs that were calculated from the ABI HVM images. The same type of plot represents an equal design size of the phase defect. The typical values of the depth and full width at half maximum of the phase defects calculated from the SPM images are also shown in Fig. 7(a). When it comes to the defect volume, the variations due to the measurement repeatability as prescribed in Sec. 3.1 were much smaller than the defect-to-defect variations. This result indicates that measuring the volume of each phase defect is important in order to evaluate the DSI or the defect detection yield.

The large variations of the DSIs as shown in error bars along the vertical axis in Fig. 7(a) were caused by the influence of the relatively large pixel size of the CCD camera. A summing up of 2 × 2 pixel (924 × 924 nm at the EUV blank plane) intensities that included the phase defects were defined as DSI values. Yamane et al.[29] reported that the 924 × 924-nm area seemed to be too large to calculate the DSI because the multilayer itself has its own roughness, and the EUV light scattered by the roughness is also captured by the Schwarzschild optics. Then to reduce the influence of the surface roughness of the multilayer on the DSI analysis, the images of each phase defect were acquired by using the 1200× review optics with an exposure time of 2 s. The DSI

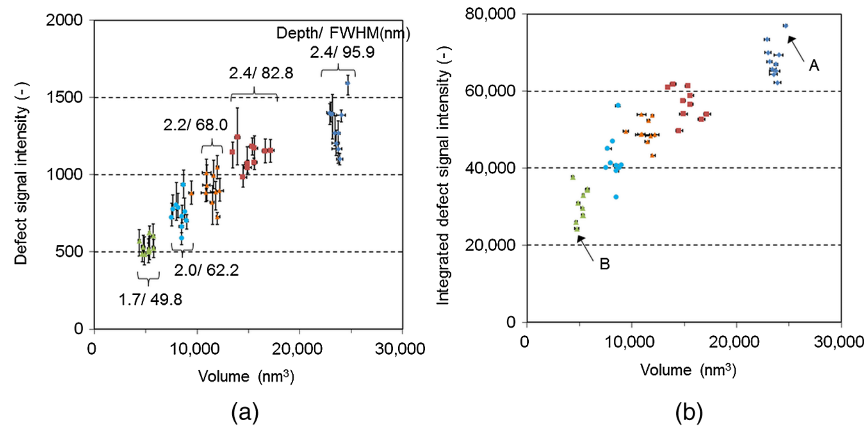

Fig. 7 Defect signal intensities as a function of the phase defect volume: (a) Using 26× inspection mode; (b) using 1200× review mode.

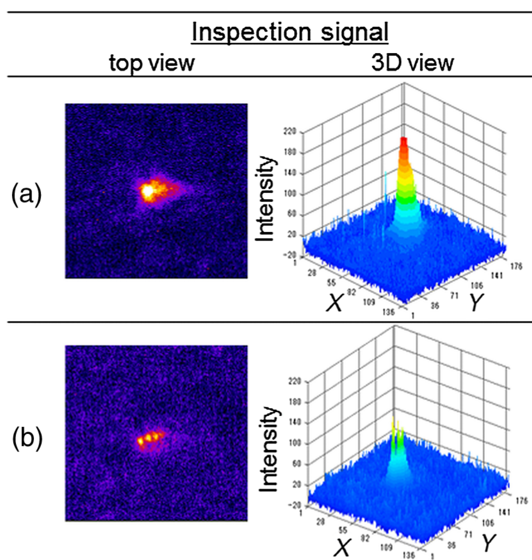

Fig. 8 Inspection signals of the phase defects A and B in Fig. 7(b).

values were calculated by integrating the pixel intensities above the back-ground level of the acquired images. Figure 7(b) represents the DSI as a function of the defect volume, and Fig. 8 shows the acquired images of the phase defects of A and B in Fig. 7(b). As shown in Fig. 8, the inspection signal showed a sharp defect signal with negligibly small noise caused by the multilayer roughness as prescribed. This result shows that the actual DSI can be measured by acquiring the defect image with the review optics and that the DSI shows a correlation with the defect volume.

4 Summary and Conclusion

The influence of the variation of the phase defect volume on the defect detection signal intensity was examined. A programmed phase defect EUV mask was fabricated for this experiment. The EUV mask consisted of programmed phase defects of 50, 60, 70, 80, and 100-nm-wide pit-type phase defects. After seeking an ideal SPM imaging condition, measurement repeatability tests of the phase defect volume were conducted. The variations of the measured volumes of 20 consecutive measurements with a single tip were larger than those of the tip-to-tip variations. The defect volume variation due to the measurement repeatability was much smaller than defect-to-defect variations. This result indicates that the measuring volume of each phase defect is essential in order to evaluate the DSI or the defect detection yield. Next, all the phase defects were measured for their volumes using SPM and images were acquired using the ABI HVM. The DSIs were calculated from the acquired images. Using 26× inspection optics, the large variations of the DSIs were observed due to the influence of the surface roughness of the multilayer, because the EUV light scattered by the roughness was also captured by the Schwarzschild optics. The actual DSI could be measured by acquiring the defect image with the review optics, where the DSI shows a correlation with the defect volume.

Acknowledgments

The authors are grateful to Hiroki Miyai and Tomohisa Ino of Lasertec Corporation for their technical advice and inspection using ABI HVM, and Takeshi Yamane and Noriaki Takagi of EIDEC for their technical advice and fruitful discussion. This work was supported by New Energy and Industrial Technology Development Organization (NEDO).

References

1. R. Jonckheere et al., "Dependence of EUV mask printing performance on blank architecture," *Proc. SPIE* **6921**, 69211W (2008).
2. N. Davydova et al., "Mask aspects of EUVL imaging at 27 nm node and below," *Proc. SPIE* **8166**, 816624 (2011).
3. T. Shoki et al., "Improvement of total quality on EUV mask blanks toward volume production," *Proc. SPIE* **7636**, 76360U (2010).
4. H. Kinoshita et al., "Mask technology of extreme-ultraviolet lithography," *Proc. SPIE* **3412**, 358 (1998).
5. Y. Arisawa et al., "Impact of EUV mask roughness on lithography performance," *Proc. SPIE* **8679**, 86792S (2013).
6. H. Aoyama et al., "Applicability of extreme ultraviolet lithography to fabrication of half pitch 35 nm interconnects," *Proc. SPIE* **7636**, 76361N (2010).
7. Y. Kikuchi et al., "Study of EUV outgassing spatial distribution toward witness plate in the EUV outgas tester," *Proc. SPIE* **8679**, 86790M (2013).
8. H. Hashimoto et al., "Development of a new mask pattern inspection tool NPI-7000 and applied results to EUV mask inspection," *Proc. SPIE* **8441**, 844117 (2012).
9. R. Hirano et al., "Evaluation of novel projection electron microscopy (PEM) optics for EUV mask inspection," *Proc. SPIE* **8679**, 86791T (2013).

10. S. Shimomura et al., "Demonstration of defect free EUV mask for 22 nm NAND flash contact layer using electron beam inspection system," *Proc. SPIE* **7969**, 79691B (2011).
11. F. Aramaki et al., "Development of new FIB technology for EUVL mask repair," *Proc. SPIE* **7969**, 79691C (2011).
12. M. Waiblinger et al., "e-beam induced EUV photomask repair: a perfect match," *Proc. SPIE* **7545**, 75450P (2010).
13. T. Amano et al., "Study of EUV mask defect repair using FIB method," *Proc. SPIE* **7823**, 782323 (2010).
14. Z. Zhang et al., "Investigation of resist effects on EUV mask defect printability," *Proc. SPIE* **6730**, 673016 (2007).
15. T. Liang et al., "EUV mask pattern defect printability," *Proc. SPIE* **6283**, 62830K (2006).
16. H. Aoyama et al., "Repair specification study for half-pitch 32-nm patterns for EUVL," *Proc. SPIE* **6730**, 67305L (2007).
17. D. V. Heuvel et al., "Natural EUV mask blank defects: evidence, timely detection, analysis and outlook," *Proc. SPIE* **7823**, 78231T (2010).
18. T. Onoue et al., "Development of fiducial marks on EUV blanks for defect mitigation process," *Proc. SPIE* **8322**, 832226 (2012).
19. T. Murachi et al., "Registration accuracy improvement of fiducial mark on EUVL mask with MIRAI EUV ABI prototype," *Proc. SPIE* **8679**, 86791U (2013).
20. T. Murachi et al., "Fiducial mark requirements from the viewpoints of actinic blank inspection tool for phase-defect mitigation on EUVL mask," *Proc. SPIE* **8522**, 85221U (2012).
21. R. Jonckheere et al., "Repair of natural EUV reticle defects," *Proc. SPIE* **8166**, 81661G (2011).
22. A. Tchikoulaeva et al., "EUV actinic blank inspection: from prototype to production," *Proc. SPIE* **8679**, 86790I (2013).
23. T. Suzuki et al., "EUV actinic blank inspection tool with a high magnification review mode," *Proc. SPIE* **8441**, 844115 (2012).
24. T. Yamane et al., "Phase defect analysis with actinic full-field EUVL mask blank inspection," *Proc. SPIE* **8166**, 81660G (2011).
25. H. Miyai et al., "The capability of high magnification review function for EUV actinic blank inspection tool," *Proc. SPIE* **8701**, 870118 (2013).
26. T. Yamane et al., "Impact of EUVL mask surface roughness on an actinic blank inspection image and a wafer image," *Proc. SPIE* **8522**, 85220H (2012).
27. N. Takagi et al., "Effect of phase defect shape on ABI signal intensity and defect image intensity on wafer with simulation," *Proc. SPIE* **8679**, 86791X (2013).
28. T. Suzuki et al., "Defect analysis on actinic blank inspection tool," *Proc. SPIE* **9256**, 92560O (2014).
29. T. Yamane et al., "Performance in practical use of actinic EUVL mask blank inspection," *Proc. SPIE* **9256**, 92560P (2014).

Tsuyoshi Amano received his BS and MS degrees in applied chemistry from Keio University in 1997 and 1999, respectively, and PhD degree in engineering from University of Hyogo in 2013. In 1999, he joined Dai Nippon Printing Co., Ltd., where he carried out research on mask process, metrology, and repair technology. Later, he was assigned to EIDEC, where he has been engaged in the development of patterned mask and blank inspection since 2011.

Biographies of the other authors are not available.